Zhang, Xu, Lai, Leijie, Li, Pengzhi ORCID logoORCID: https://orcid.org/0000-0001-8883-1885 and Zhu, Li-Min (2022) Data-driven fractional order feedback and model-less feedforward control of a XY reluctance-actuated micropositioning stage. Review of Scientific Instruments, 93. Art 115002. doi:10.1063/5.0098759

Official URL: https://doi.org/10.1063/5.0098759
DOI: http://dx.doi.org/10.1063/5.0098759
EPrint URI: https://eprints.glos.ac.uk/id/eprint/11903

Data-driven fractional order feedback and model-less feedforward control of a XY reluctance-actuated micropositioning stage

Xu Zhang,[1] Leijie Lai[1,a)], Pengzhi Li[2,a)] and Li-Min Zhu[3]

[1)] *School of Mechanical and Automotive Engineering, Shanghai University of Engineering Science, Shanghai 201620, China.*

[2)] *School of Computing and Engineering, University of Gloucestershire, Cheltenham, GL50 2RH, UK*

[3)] *State Key Laboratory of Mechanical System and Vibration, Shanghai Jiao Tong University, Shanghai 200240, China*

(Dated: 13 September 2022)

This paper proposes a compound data-driven control method to solve the problems of low damping resonance, different dynamics properties and hysteresis in the large-range compliant micropositioning stage driven by Maxwell reluctance actuator. Firstly, in order to verify the proposed control algorithm, a reluctance-actuated XY compliant micropositioning stage is constructed according to the principle of reluctance actuator. Secondly, in order to eliminate the influence of complex dynamics on the controller design, a fractional order proportional-integral (FOPI) feedback controller is designed by using data iterative feedback turning (IFT) algorithm. Thirdly, the FIR feedforward filter is optimized by using the experimental data, and the online inverse estimation of the system frequency response function and its iterative feedforward compensation are carried out to further eliminate the influence of light damping resonance. Finally, the proposed control method is used for tracking experiment and compared with other methods. The experimental results show that the proposed control method can better meet the requirements of high precision, fast speed and strong anti-interference ability for large stroke micro/nano positioning and tracking.

[a)] The authors to whom correspondence may be addressed: lailj@sues.edu.cn, kindrobot@163.com

I. INTRODUCTION

Micro/nanoprecision motion and positioning technology demonstrates extensive and significant applications in the fields of micro/nanomanufacturing and measurement such as nanolithography, ultraprecision machining and scanning probe microscope, etc[1–3]. With the continuous development of these fields, large stroke and high dynamic micro/nanopositioning stage has rapidly become the research frontier and hotspot in the field of precision engineering because of its comprehensive performance and large application scope[4,5]. Taking linear motion as an example, large stroke nanopositioning usually refers to the ability to achieve nanometer-resolution or positioning accuracy ($0.1 \sim 100$ nm) within millimeter stroke, which requires an integrated design of sensing, guidance and driving. However, the applications of several common linear actuators in large stroke micropositioning stage are limited by their own characteristics. For example, the stage driven by piezoelectric actuator (PZT) has nanopositioning accuracy, but its stroke is generally only tens of microns, which can only be hundreds of microns at most even if displacement is amplified by the amplification mechanism. Moreover, it is difficult to balance control bandwidth and stroke range[6]. In spite of advantages such as low disturbance, high resolution and large motion range, voice coil motor (VCM) can provide limited acceleration due to its low efficiency, high power consumption and insufficient thrust.

Recently, a kind of normal-stressed electromagnetic actuator, also known as Maxwell reluctance actuator, has gradually become a research hotspot in the field of micro/nanopositioning due to its excellent dynamic performance[7]. Different from the VCM driven by lorentz force, the reluctance actuator generates variable reluctance normal stress based on the principle of minimum reluctance. The generated thrust is directly proportional to the square of the passing current, so it can generate a larger thrust with a smaller current. Moreover, excitation coils are wound on the stator of the reluctance actuator, providing great thrust density, low inertia, fast response speed, simple structure and strong heat load capacity for the actuator. However, the complex dynamic characteristics brought by its large air gap of the reluctance actuator seriously limit its application in large stroke micro/nanopositioning stage despite its obvious advantages[8,9].

Because of high economy and easy implementation, it has become a mainstream trend to design an effective controller to solve the problems caused by complex dynamic characteristics. At present, many methods have been developed to solve this problem, like adaptive control, sliding mode control, $H\infty$ control, and inversion-based technique[10,11]. For example, Ito et al. designed a PI-based feedback controller containing a notch filter and a lead compensator to enable high-precision long-stroke motion of a flexure-guided nanopositioner with reluctance actuator[12]. Tian et al. proposed a sliding mode control with proportion integration differentiation (PID) sliding surface to control the XY micro/nanopositioning stage driven by two VCMs[13]. Wang et al. proposed a simultaneous optimization approach for a dual-loop controller consisting of an inner loop positive acceleration, velocity, and position feedback (PAVPF) damping controller and an outer loop PI tracking controller[14].

Traditional model-based control methods have been widely used in the PZT and VCM actuated nanopositioning stage, but it is difficult to meet the control requirements of such reluctance-actuated micropositioning stage due to their characteristics of position-dependent dynamics and hysteresis[15–18]. For instance, when the model-based feedforward control is used, the tracking performance is limited in practice due to the unavoidable model uncertainty, modeling error, and nonminimum phase zeros[19]. Therefore, data-driven control strategy that can eliminate the influence of the model has become a preferred control strategy to improve the performance of the positioning system. For example, Awtar et al. attempted to control micropositioning system using iterative learning control (ILC) and feedforward control[20]. However, the ILC technique is sensitive to the resonance vibration of flexure mechanism and set-point variations, thus limiting its application in reluctance-actuated compliant micropositioning stage.

In order to solve the problems existing in the above control methods and obtain better tracking performance, a data-driven compound feedback/feedforward control method is proposed in this paper. Firstly, a fractional order PI controller is designed by using iterative feedback tuning (IFT) algorithm to eliminate the tracking error and improve the stability and robustness of the stage. After that, the error is eliminated by a model-free finite impulse response (FIR) filter based on nonparametric frequency domain system identification. And then, a modeling-free inversion-based iterative feedforward control (MIIFC) is used to iterate all frequencies in the tracking signal to eliminate the periodic error more thoroughly. Finally, a comparative experiment of trajectory tracking is carried out. The results show that the proposed control method outperforms the conventional control methods in eliminating periodic and aperiodic errors, which proves the effectiveness of the proposed controller. The main contribution and innovation of this work is the successful application of data-driven and model free controller in large stroke micropositioning system driven by reluctance actuator with complex dynamic characteristics. In addition, the proposed reluctance-actuated micropositioning stage can be an alternative for the large stroke micro/nanopositioning technology in micro/nanomanufacturing fields such as fast tool servo (FTS) system and photolithography machine.

II. SYSTEM DESCRIPTION

Fig. 1 (a) shows the large stroke reluctance-actuated micropositioning stage designed based on Maxwell normal stress. The working principle of the electromagnetic actuator and its magnetic flux distribution is illustrated in Fig. 1 (b), while the decoupled XY flexure mechanism of the stage is shown in Fig. 1 (c). It can be seen from the figures that two electromagnetic actuators are arranged in parallel and connected with the input stage of the flexure mechanism. As illustrated in Fig. 1 (b), the reluctance actuator consists of a magnetic yoke, a mover, a Nd-Fe-B permanent magnet, and two identical excitation coils. The excitation coil provides the excitation magnetic field required by the actuator, while the permanent magnet provides the direct-current (DC) bias magnetic fluxt, whose directions in the left and right air gaps between the mover and the yoke are opposite. Both the yoke and the mover made of layered Fe-based amorphous alloy, provide the corresponding magnetic circuit for magnetic conduction. By superimposing the coils' flux onto the magnet's flux, the mover can be subjected to differential Maxwell electromagnetic normal stress, producing the driving force and making the actuator move with the driving current. The driving force F has a nonlinear relationship with excitation current and mover position, which can be expressed by

$$F = K_{\mathrm{m}} I + k_{\mathrm{a}} x, \tag{1}$$

where K_{m} and k_{a} represent the motor constant and the actuator stiffness, and x is the mover position from the center[12]. The detailed design of the electromagnetic actuator and the stiffness of the flexure mechanism can be referred to in our previous articles[21]. In this 2-DOF flexure mechanism, the length l, width b and height h are respectively 63 mm, 1.4 mm, 15 mm and the stiffness in the X/Y directions can be calculated as $k = 6Ebh^3/l^3$, which is equal to 60 N/mm.

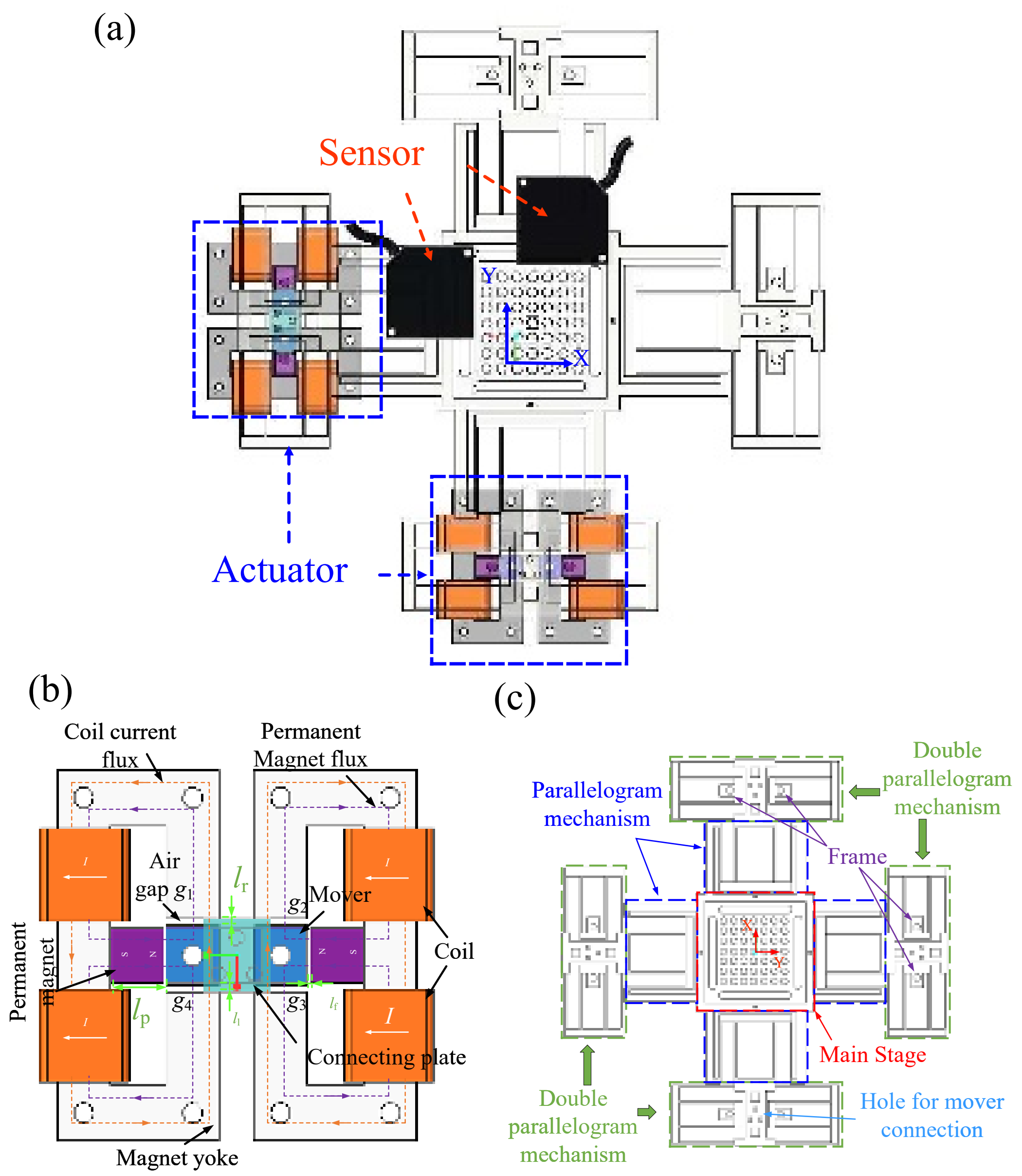

FIG. 1. Large stroke micropositioning system based on the Maxwell reluctance actuator. (a) Schematics of micropositioning system. (b) Magnetic circuit. (c) Main structure of XY flexure mechanism

A hardware in the loop simulation system based on a real-time control board (LinksBox-02 from Beijing LinksTech) was constructed to verify the control performances of the micropositioning stage. A linear amplifier (CH808 form HIT-UOI) was used to linearly convert the output voltage (-10 ∼ 10 V) into the coil current (−8 ∼ 8 A). Two laser displacement sensors (HL-G103-S-J from Panasonic) were employed to measure the stage

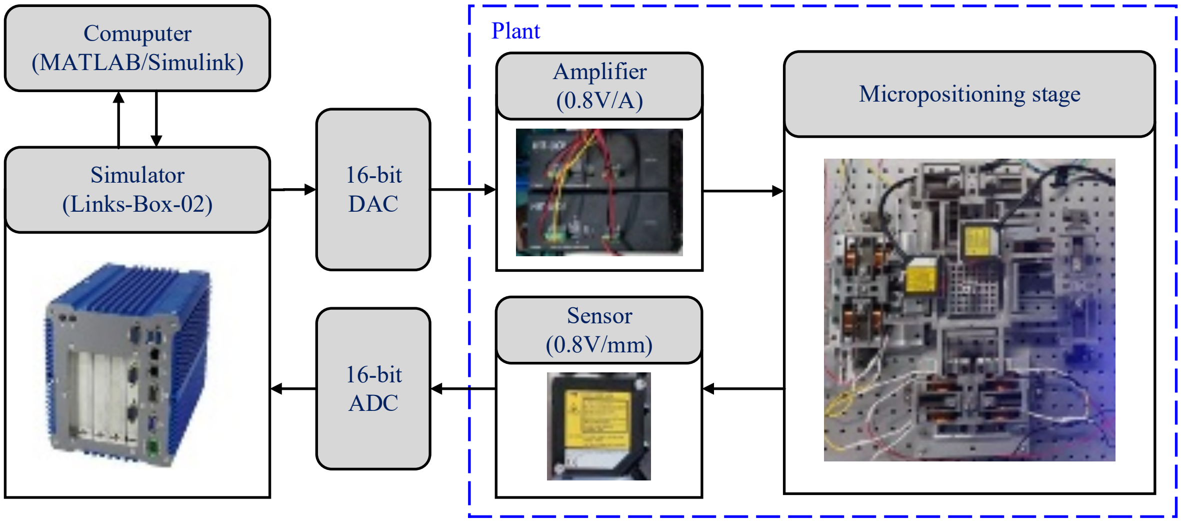

FIG. 2. Hardware layout of micropositioning stage

displacements, which had a measurement range of ±4 mm corresponding to the analog output of $0 \sim 10$ V. The linearity and sampling rate of the displacement sensor are ±0.1% in full scale, and 200 μs, respectively. A data acquisition card (PCI-6221 from NI) equipped with 16-bit A/D and D/A converters was utilized to acquire the sensor voltage ($0 \sim 10$ V) and to apply the control voltage ($-10 \sim 10$ V) to the linear amplifier. The data acquisition card communicates with the real-time control board through PCI bus. The hardware layout of micropositioning stage is shown in Fig. 2.

III. DATA DRIVEN FEEDBACK CONTROLLER

As illustrated in Eq. (1), the actuator's nonlinear negative stiffness K_a can offset part of the stiffness k of the flexure mechanism, thus reducing the current while increasing energy efficiency of the large stroke stage, which, however, makes the dynamic characteristics of the stage more complex. Moreover, the nonlinearities of magnetic flux leakage and hysteresis also affects the control accuracy of the stage.

Aiming at the complex dynamic characteristics and hysteresis nonlinearity, a data-driven compound control strategy including model-free FIR filter, MIIFC and fractional order PI (FOPI) controller is proposed. The schematic diagram is shown in Fig. 3. Among them, the FOPI controller adjusted by IFT algorithm provides sufficient stability margin and robustness for the system. FIR and MIIFC are designed for the nonlinear compensation and error elimination of the stage. Their specific design will be discussed in section IV.

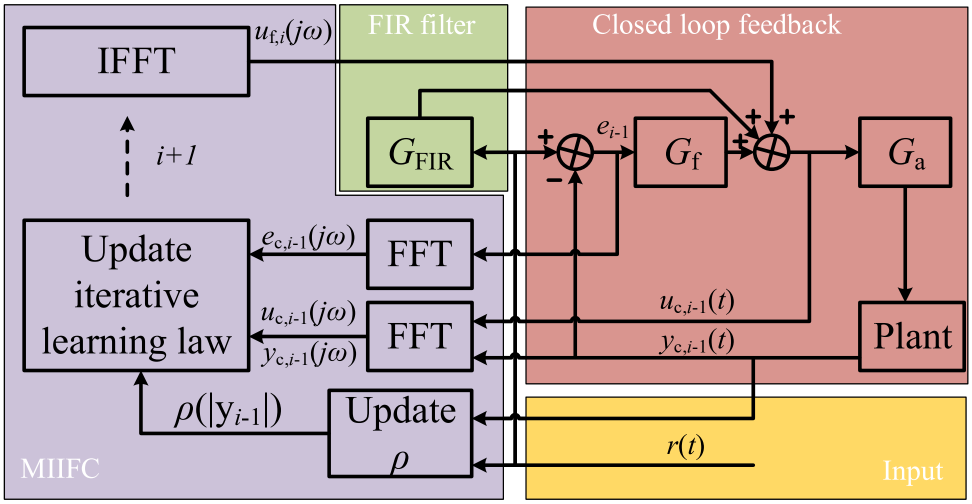

FIG. 3. Schematic diagram of data-driven compound control of large stroke positioning stage

A. Fractional order PI controller

As one of the most frequently used controllers, PI controller cannot flexibly adjust the steady-state margin of the flexure-based micropositioning stage with light damping due to its own structural constraints, which results in the contradiction between tracking speed and stability of the stage.

In contrast, the improved FOPI controller can adjust the phase and amplitude margin more flexibly due to the introduction of fractional order parameters[22]. The specific FOPI controller G_f is defined as:

$$G_f = \frac{K_p s^{\alpha} + K_i}{s^{\beta}}, \tag{2}$$

where K_p and K_i are proportional gain and integral gain respectively, and α and β are the order of zeros and poles respectively. It can be seen that compared with integer order PI (IOPI) controller, the FOPI adds integral order parameters β and derivative order parameter α. Therefore, the controller can adjust the amplitude margin and phase margin of the system more flexibly, effectively improving the stability, rapidity and robustness of the stage[22,23].

Fig. 4 shows the effects of different integral and derivative parameters on the amplitude and phase of the FOPI controller. It can be seen from Fig. 4 (a), that the slope of amplitude curve and phase of FOPL controller change with zero order α and pole order β,

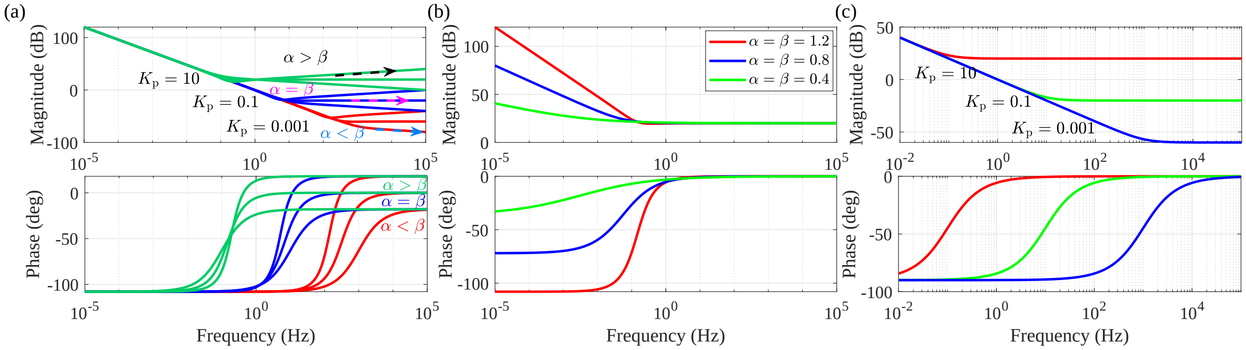

FIG. 4. Effects of different zero and pole orders on the amplitude and phase of controller. (a) Influence of the relationship between α and β on FOPI controller. (b) The FOPI controller change with α and β. (c) Integer order PI controller

which can be flexibly selected for different control objects. When the system has no strict requirements for reducing high-frequency noise and needs enough phase margin to provide sufficient robustness, $\alpha > \beta$ can be selected. If the system is stable enough, it is necessary to suppress the noise. On the premise of maintaining the stability of the system, $\alpha < \beta$ should be selected carefully. When no special requirements are made, $\alpha = \beta$ can be selected to obtain the required control performance and greatly simplify design steps. Based on the above analysis, the zero order α of FOPI controller is the same as the pole order β.

Fig. 4 (b) shows the influence of different values on FOPI when zero and pole orders are equal. If the values of proportional gain K_p, and integral gain K_i are the same, the gain of FOPI controller for low-frequency signal increases with the zero order α and pole order β. Moreover, the phase also breaks through the limitation of the traditional integration link, which does not have to start from -90°, and can start from different phases by adjusting α and β. And by comparing Fig. 4 (b) and Fig. 4 (c), it can be seen that even after the parameter $\alpha = \beta$ is selected, the fractional order controller still has the ability to adjust the phase and amplitude more flexibly than the integer order controller, which also means that it has better control performance.

According to the above analysis, the FOPI controller is sensitive to the order of zero order α and pole order β which affect the positioning and tracking accuracy of the stage. In order to eliminate the stage's inconsistent dynamic models and identification accuracy in FOPI controller design, FOPI controller is designed by using data-driven IFT algorithm in the next section.

B. Controller Parameters Optimization Based on IFT Algorithm

As a design method to find the optimal parameters of the controller by using the measured data and gradient iteration, IFT is mainly used in the controller design of linear time invariant closed-loop system. The main aim of IFT is to reduce the cost function value, represented by Eq. (3), through the iteration of the controller parameter vector, to eventually optimize the controller parameters.

$$J({}^{i}\boldsymbol{\rho}) = \psi_1 e({}^{i}\boldsymbol{\rho})^{\mathrm{T}} \cdot e({}^{i}\boldsymbol{\rho}), \tag{3}$$

where ψ_1 is the weight coefficient, whose value is 0.5 times the reciprocal of the data length, ${}^{i}\boldsymbol{\rho}$ is the parameter matrix obtained in the iteration, and $e({}^{i}\boldsymbol{\rho})$ is the tracking error between the desired output y_{d} and the actual output y_{r} in the ith iteration, $J({}^{i}\boldsymbol{\rho})$ is the cost function. In order to ensure that the value of the cost function decreases with iteration, the Levenberg-Marquardt algorithm is used in the iteration

$$\begin{aligned} {}^{i+1}\boldsymbol{\rho} &= {}^{i}\boldsymbol{\rho} - \xi_i(\boldsymbol{H}_i+\mu\boldsymbol{I})^{-1} \cdot \nabla^{i} J({}^{i}\boldsymbol{\rho}) \\ \boldsymbol{H}_i &= [\nabla^{i} y_r({}^{i}\boldsymbol{\rho})]^{\mathrm{T}} \cdot [\nabla^{i} y_r({}^{i}\boldsymbol{\rho})]. \end{aligned} \tag{4}$$

Both ξ_i and μ are positive numbers and affect the convergence rate, which need to be selected in combination with the actual situation. $\boldsymbol{H}_i$ is the approximate matrix of the cost function $J(\boldsymbol{\rho})$, calculated from the experimental data, to the Hessian matrix of the controller parameter vector $\boldsymbol{\rho}$, and $\boldsymbol{H}_i^{-1}$ is its inverse matrix. According to Eq. (4) the partial derivative $\nabla^{i} J({}^{i}\boldsymbol{\rho})$ directly affects the iteration process

$$\nabla J({}^{i}\boldsymbol{\rho}) = 2\psi_1 e({}^{i}\boldsymbol{\rho})^{\mathrm{T}} \cdot e({}^{i}\boldsymbol{\rho}) \nabla^{i} y_r({}^{i}\boldsymbol{\rho}). \tag{5}$$

Since the actual output y_{r} and the desired output y_{d} can be directly obtained from the experimental data, as shown in Eq. (5), only the $\nabla^{i} y_r({}^{i}\boldsymbol{\rho})$ needs to be calculated. However the system model is unknown. To solve this problem, a method to calculate the gradient $\nabla^{i} y_r({}^{i}\boldsymbol{\rho})$ without system model in IFT algorithm is proposed. To facilitate understanding, we substitute the derivative of the closed-loop transfer function of the system into the s domain

$$\nabla^{i} y_{\mathrm{r}}({}^{i}\boldsymbol{\rho}) = \nabla^{i} G_{\mathrm{f}}({}^{i}\boldsymbol{\rho}) \cdot \frac{1}{G_{\mathrm{f}}({}^{i}\boldsymbol{\rho})} \cdot \frac{G_{\mathrm{f}}({}^{i}\boldsymbol{\rho}) P}{(1+G_{\mathrm{f}}({}^{i}\boldsymbol{\rho})P)^2} \cdot y_{\mathrm{d}}, \tag{6}$$

where $P(\cdot)$ is the transfer function of the stage. Since the last term in Eq. (6) is a transfer function from input y_d to error e, it can be simplified as:

$$\nabla^i y_\mathrm{r}({}^i\boldsymbol{\rho}) = \nabla^i G_\mathrm{f}({}^i\boldsymbol{\rho})\frac{1}{G_\mathrm{f}({}^i\boldsymbol{\rho})}\frac{G_\mathrm{f}({}^i\boldsymbol{\rho})P}{1+G_\mathrm{f}({}^i\boldsymbol{\rho})P}e. \tag{7}$$

To summarize, the IFT algorithm estimates the derivative $\nabla^i y_\mathrm{r}({}^i\boldsymbol{\rho})$, using Eqs. (6) and (7). It is worth noting that the selection of ξ_i in Eq. (4) directly affects the stability of the algorithm.

We should be aware of two issues in the use of IFT algorithm. One is that, ξ_i should be selected according to the actual situation, but it still needs to meet the convergence condition $\sum\limits_{i=1}^{\infty}\xi_i = \infty, \sum\limits_{i=1}^{\infty}\xi_i^2 < \infty$. Under this condition, the IFT algorithm can converge to the local minimum. Huusom et al. also gave different suggestions, that is, let $\xi_i = a_j/i, j = 1, 2, \cdots 3$, because $\sum\limits_{i=1}^{\infty}\frac{a_j}{i} = \infty, \sum\limits_{i=1}^{\infty}\left(\frac{a_j}{i}\right)^2 = \frac{a_j^2\pi^2}{6} < \infty$. In addition, $\boldsymbol{a} = [a_1, a_2, a_3]$ becomes a vector composed of each parameter iteration step, where the controller parameters are different convergence rates. The other significant issue is the IFT algorithm that uses the system input and output data to iterate the parameters of the controller, so it is necessary to know the partial derivatives of the controller transfer function for different parameters so as to eliminate the influence of complex parameters such as fractional order parameters on IFT algorithm in the design process of fractional order controller. Oustaloup et al. proposed to approximate fractional calculus operators with finite integer order transfer functions[24]. The bounded differential transfer function $C_0\frac{1+s/\omega_\mathrm{b}}{1+s/\omega_\mathrm{h}}, \omega_\mathrm{b} \ll \omega_\mathrm{A}, \omega_\mathrm{h} \gg \omega_\mathrm{B}$ is used to limit the differential transfer function s/ω_u to the frequency range $[\omega_\mathrm{A}, \omega_\mathrm{B}]$, and the equivalent finite dimensional transfer function is used to approximate $D(s)$. Now, $\omega_\mathrm{u} = \sqrt{\omega_\mathrm{b}\cdot\omega_\mathrm{h}}$ and $C_0 = \omega_\mathrm{b}/\omega_\mathrm{u}$. Next, a recursive distribution composed of a large number of real poles and zeros is as follows:

$$D(s) = \lim_{x\to\infty}\left(\frac{\omega_\mathrm{u}}{\omega_\mathrm{h}}\right)^{\alpha}\prod_{i=-N}^{N}\left(\frac{1+s/{\omega'}_i}{1+s/\omega_i}\right)^{\alpha} \tag{8}$$

where, ω_h and ω_b determine the definition domain of $D(s)$ after approximation, and N determines the $D(s)$ approximation accuracy. Theoretically, the larger N, the higher the approximation accuracy. However, larger N values will result in the generation of excessive poles and zeros in $D(s)$ and increase the calculation time. Therefore it should be selected in combination with the actual situation. In this paper, $\omega_\mathrm{b} = 2\pi\cdot 0.00001$ rad/s, $\omega_\mathrm{h} = 2\pi\cdot 10000$ rad/s, $N = 5$.

In summary, the details of IFT algorithm of fractional phase-lead PI controller is as follows:

step 1. Set the iteration parameter $i = 0$ and select the initial controller parameter ρ_o.

step 2. Experiment 1: select y_{d} as the input signal, measure the output y_{r}^1, and calculate the tracking error $e = y_{\mathrm{d}} - y_{\mathrm{r}}^1$.

step 3. Experiment 2: select E as the input signal and measure the system output y_{r}^2.

step 4. Complete the controller approximation based on section III part B.

step 5. Calculating the partial derivative vector $\nabla^i y_{\mathrm{r}}({}^i\boldsymbol{\rho})$ of the closed-loop output, y_{r} to the controller parameters, based on Eq. (6).

step 6. Calculate $\nabla J({}^i\boldsymbol{\rho})$, based on the Eq. (4).

step 7. Update the parameter vector ${}^i\boldsymbol{\rho}$.

step 8. Update the parameters in the controller for Experiment 1. Calculate the value of the cost function at this time and judge whether it meets the termination conditions. If so, the iteration stops. Otherwise, repeat steps 2-7.

IV. DATA-DRIVEN FEEDFORWARD CONTROLLER

Feedforward control is often used in conjunction with feedback control to improve the control performance of the stage. As a model-free filter, FIR filter stands out from many feedforward controllers because it is able to find an accurate model without the use of system identification method, overcoming the difficulties related to non-minimum phase zero inversion. In this paper, FIR filter is also used as feedforward controller, and its parameters are obtained by using frequency domain data. Furthermore, the frequency domain inverse iterative learning control is used to reduce the impact of periodic interference on the stage.

A. FIR filter

The model-free FIR filter is designed based on nonparametric frequency domain system identification to generate empirical transfer function estimation (ETFE) matrix[25]. Then the FIR filter is synthesized directly using the measured frequency response[26]. The accuracy of FIR filter mainly depends on the number of taps, and its transfer function is expressed as:

$$F(z^{-1}) = z^{q}(c_0 + c_1 z^{-1} + \ldots + c_{p-1} z^{-p+1}) = z^{q}\boldsymbol{c}^{\mathrm{T}}\boldsymbol{z}, \tag{9}$$

where $p, q \in \boldsymbol{N}_0$, $\boldsymbol{c} = [c_0, c_1, \ldots c_{p-1}]^{\mathrm{T}}$ and $z = [1, z^{-1}, \ldots, z^{-p+1}]^{\mathrm{T}}$.

In addition, the filter length p must be selected in combination with the actual situation, and q can be calculated by:

$$q = \begin{cases} p/2, \text{ if } p \text{ is even} \\ (p+1)/2, \text{if } p \text{ is odd} \end{cases} \tag{10}$$

The coefficient matrix $\boldsymbol{c}$ in Eq. (9) is obtained by minimizing the weighted least squares cost function of error e

$$e(k) = F(e^{-j2\pi k/M}) - H(k) = \boldsymbol{c^T}\boldsymbol{x}_k - H(k). \tag{11}$$

Using $z = e^{j2\pi k/M}$, we obtain

$$\boldsymbol{x}_k = [e^{-j\frac{2\pi k(-q)}{M}}, e^{-j\frac{2\pi k(1-q)}{M}}, \ldots, e^{-j\frac{2\pi k(p-q)}{M}}], \tag{12}$$

where, M is the number of samples in a period, that is, the minimal standard weighted linear least squares cost function is

$$J(\boldsymbol{c}) = \sum_{k=0}^{M-1} W(k)e(k)e^{*}(k) = \left\|\boldsymbol{W}^{1/2}(\boldsymbol{b} - \boldsymbol{X}\boldsymbol{c})\right\|^{2}. \tag{13}$$

And

$$\boldsymbol{W} = \mathrm{diag}([W(0), W(1), \ldots, W(M-1)]), \tag{14}$$

$$\boldsymbol{b} = \begin{bmatrix} H(0) \\ H(1) \\ \vdots \\ H(M-1) \end{bmatrix}, \boldsymbol{X} = \begin{bmatrix} x_0^{\mathrm{T}} \\ x_1^{\mathrm{T}} \\ \vdots \\ x_{M-1}^{\mathrm{T}} \end{bmatrix} \tag{15}$$

where $\boldsymbol{W} \in \boldsymbol{R}^{M\times M}$ is an error weighting function, $\boldsymbol{b} \in \boldsymbol{R}^{M\times 1}, \boldsymbol{X} \in \boldsymbol{R}^{M\times M}$. Note that $H\left(k\right) = \left(\frac{Y(k)}{U(k)}\right)^{-1}$ is the inverse response of the plant from input to output. The error weighting function can be used to adjust how to weigh the error at different frequencies. Here, a unit weight is used, i.e. $W(k) = 1$. The *Matlab* function *lscov* can be used to minimize Eq. (13).

B. Modeling-free inversion-based iterative feedforward control

In order to further eliminate the periodic error and the influence of the complex dynamic characteristics of the system, the MIIFC is used to iterate all frequencies in the tracking signal. Generally, based on previous literature, for linear time invariant systems (LTI) systems, the influence of nonlinearity can be regarded as interference. For any $u_{\mathrm{c}} \neq 0$, the control law of MIIFC can be expressed as:

$$\begin{aligned} & e_i(j\omega) = r(j\omega) - y_i(j\omega) \\ & u_{\mathrm{c},i}(j\omega) = \begin{cases} \varrho r(j\omega), i = 0 \\ u_{\mathrm{c},i}(j\omega) + \frac{u_{\mathrm{c},i-1}(j\omega)}{y_{i-1}(j\omega)} e_{i-1}(j\omega), i \geq 1 \end{cases} \end{aligned} \tag{16}$$

where, $r(\cdot)$ is the reference trajectory, and ϱ is the constant representing the reciprocal of DC gain. e_i is the error signal calculated by the output signal y_i and the input signal r in the ith iteration. The plant of stage is inversed in frequency domain via collected data in each iteration, and $u_{\mathrm{c},i}$ is updated from the control input and tracking error signals of the previous iterations by using the estimated inverse dynamics. Consequently, the tracking performance would be consequently improved during iteration.

In practical application, considering the influence of interference on output, the actual displacement is expressed as:

$$y_i(j\omega) = P(j\omega) u_{\mathrm{c},i}(j\omega) + y_{\mathrm{n},i}(j\omega) \tag{17}$$

where $y_{\mathrm{n},i}(\cdot)$ represents the output disturbance mainly caused by nonlinearity and input-output noise in the ith iteration. Generally, the output disturbance is a bounded function, that is, $|y_{\mathrm{n},i}(\cdot)| \leq |\delta(\cdot)|$

The output disturbance of large stroke micropositioning stage is usually trail-variant during iterations, and its change rate can be expressed as:

$$\Delta\delta(j\omega) \triangleq \max_{i>0} \left| y_{\mathrm{n},i}(j\omega) - y_{\mathrm{n},i+1}(j\omega) \right|. \tag{18}$$

Thus, $\Delta\delta \leq 2\delta$ can be obtained. In order to improve the tracking performance through iterative learning control, the disturbance/noise signal ratio (NSR) should be bounded[27], i.e.,

$$\left| \frac{y_{\mathrm{n},i}(j\omega)}{r(j\omega)} \right| < 1 - \frac{\sqrt{2}}{2}, \forall i. \tag{19}$$

Nevertheless, when the ratio of the output disturbance to the reference signal is close to 1, the tracking performance will still be affected. For example, when the positioning task is performed with a smaller output $r(\cdot)$, the unknown interference $y_{\mathrm{n},i}(\cdot)$ will seriously affect the actual output $y_i(\cdot)$ and the control quality of MIIFC. As the learning gain in Eq. (16) is directly proportional to the reciprocal of $y_i(\cdot)$, the obvious fluctuation would lead to an unbounded input update, thus deteriorating the tracking performance.

A possible solution to this problem is to use the learning gain function to limit the input amplification,

$$\rho(|y_i|) = \begin{cases} 1, |y_i(j\omega)| > |r_i(j\omega)| \\ \frac{1}{2} - \frac{1}{2}\cos\,(\pi\frac{|y_i(j\omega)|}{|r_i(j\omega)|}), |y_i(j\omega)| \leq |r_i(j\omega)|. \end{cases} \tag{20}$$

And, the learning rate is updated as:

$$u_{\mathrm{c},i}(j\omega) = \begin{cases} \alpha r(j\omega), i = 0 \\ u_{\mathrm{c},i}(j\omega) + \rho(y_{i-1})\frac{u_{\mathrm{c},i-1}(j\omega)}{y_{i-1}(j\omega)} e_{i-1}(j\omega), i \geq 1. \end{cases} \tag{21}$$

The change of ρ with the increase of $|y_i(j\omega)|\,/\,|r_i(j\omega)|$ is shown in Fig. 5. It can be concluded that the boundary condition of the learning gain function can be expressed as:

$$\begin{aligned} &\inf \rho(|y_i|) \overset{\Delta}{=} \rho > 1 - \tfrac{1}{\lambda} \\ &\sup \rho(|y_i|) \overset{\Delta}{=} \bar{\rho} \leq 1, \end{aligned} \tag{22}$$

where $\lambda > 0$.

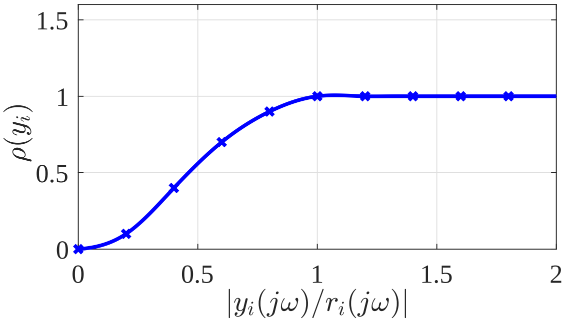

FIG. 5. Plot of learning gain function

V. EXPERIMENTS

In this section, the parameters of FOPI and FIR filter are optimized by using the input and output data, and together with MIIFC, a data-driven compound controller of large stroke micropositioning stage is established. In order to verify the effectiveness of the proposed controller and evaluate the tracking performance of the stage, a sinusoidal signal with amplitude of 2.5 V and frequency of 5 Hz is selected as the input signal in the comparative experiment between the proposed controller and other control methods. Then, to further verify the performance of the proposed compound controller, the triangular wave signals with amplitude of 2.5 V and frequency of 5 Hz and 10 Hz are tracked by the micropositioning stage. Finally, to comprehensively verify the performance of the designed 2-DOF micropositioning stage, tracking tests were conducted on complex trajectories such as concentric circle, as shown in Fig. 10.

A. Parameter optimization of FOPI and FIR filter

To simplify the complex approximation and IFT algorithm operation, *Simulink*, and the fractional order toolbox *fomcon* in *MATLAB* were used to calculate $\nabla^i y_{\mathrm{r}}({}^i\boldsymbol{\rho})$. The fractional order transfer function module in *fomcon* was used to represent the partial derivative of the controller parameters in s domain. At the same time, taking e as the input, $\nabla^i y_{\mathrm{r}}({}^i\boldsymbol{\rho})$ was calculated by using *Simulink* program. And in order to ensure the enforceability of the IFT algorithm in any situations, the initial value of controller parameter ${}^0\rho$=[${}^0K_{\mathrm{p}}$,${}^0K_{\mathrm{i}}$,${}^0\alpha$,${}^0\beta$] is obtained based on the design method of ordinary PI controller and manual adjustment. On the other hand, the chrip signal, which can fully reflect the frequency domain characteristics of the system, is selected as the identification signal of the FIR filter to complete the identification of the filter parameters. The specific parameters are given in Table I.

TABLE I. Coefficients of FIR filter

Parameter	p	c_0	c_1	c_2	c_3	c_4	c_5	c_6	c_7	c_8	c_9
Value	10	1.19	1.07	0.94	0.81	0.53	0.41	0.96	4.07	1.75	2.04

The convergence process of controller parameters is shown in Fig. 6. It is worth mentioning that to prevent noise from influencing the IFT algorithm, and to improve the convergence speed and accuracy, a zero-phase filter, based on a chebyshev type 1 filter, with an upper passband loss of 0.2 dB and cut-off frequency of 10 Hz, was used to process the experimental data with the help of the *Matlab* function *filtfilt*.

As shown in Fig. 6 (a), the controller parameters are close to the final value after one iteration, and the controller parameters gradually converge in the next four iterations. The selection of the step vector is satisfactory. Fig. 6 (b) shows the iterative process of solving the optimal FIR filter using the least square principle.

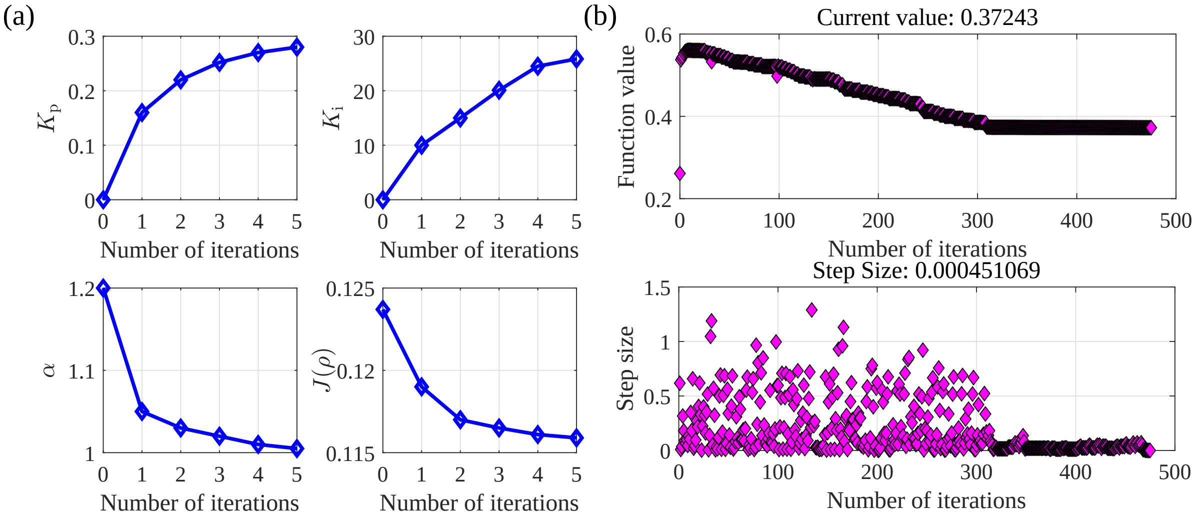

FIG. 6. Controller parameter convergence diagram. (a) Parameter variations of FOPI controller. (b) Optimization process of FIR filter.

B. Trajectory Tracking Experiment

In the comparative experiment, triangular wave signals with amplitude of 2.5V (2mm) and frequency of 10 Hz were tracked by the proposed compound controller. Compared with other controllers, the proposed controller can eliminate periodic and aperiodic tracking errors, which reflects its excellent control ability on the large stroke micropositioning stage with inconsistent dynamic characteristics. The experimental results and error analysis are shown in Fig. 7.

As can be seen from Fig. 7, FOPI controller has better positioning and tracking performance than IOPI feedback controller, because it can flexibly adjust the amplitude and phase margin of the stage. Moreover, FIR and MIIFC can eliminate the hysteresis nonlinearity of the actuator and reduce the tracking error of the stage simultaneously. More importantly,

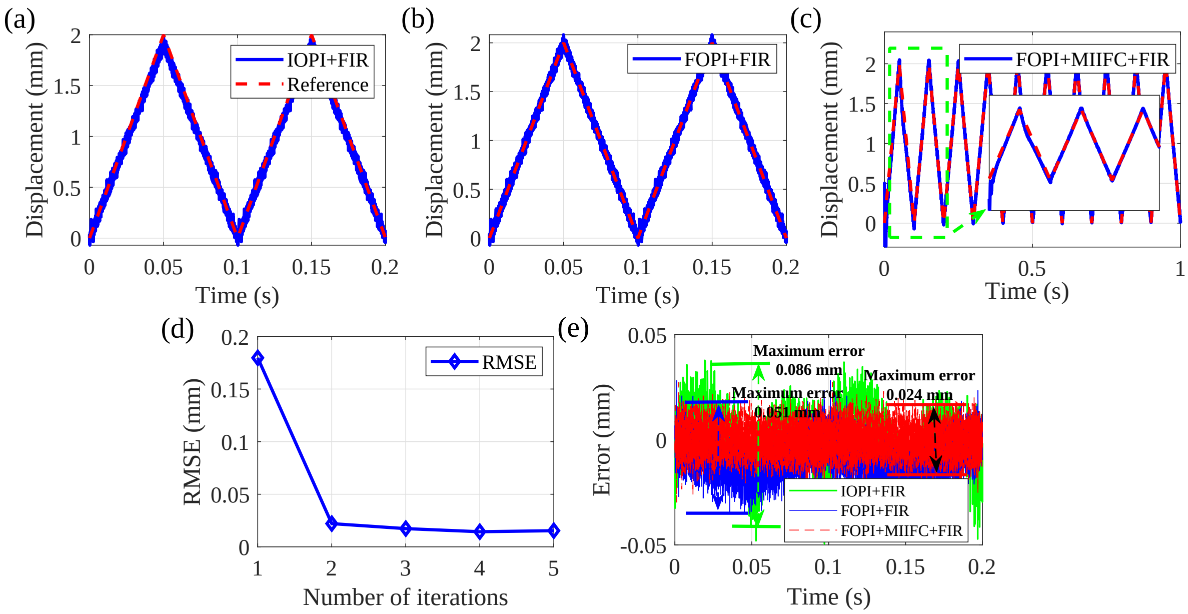

FIG. 7. Tracking results and error comparison of different controllers. (a) Tracking results of IOPI+FIR controller. (b) Tracking results of FOPI+FIR controller. (c) Tracking results of FOPI+FIR+MIIFC controller. (d) Convergence effect of root mean square (RMSE) errors using FOPI+FIR+MIIFC controller. (e) Comparison of tracking errors of different controllers

the iteration speed of MIIFC can be effectively increased by using the FIR filter. In addition, the error analysis in Fig. 7 shows that although the FIR filter as feedforward can effectively improve the tracking performance of the stage, its suppression of periodic error still needs to be strengthened. With the introduction of MIIFC, the periodic error is greatly reduced. Compared with FOPI controller and FOPI + FIR controller, the tracking errors of the proposed compound controller are reduced by 72.1% and 53% respectively.

To further verify the strong robustness and high accuracy of the proposed control method on the stage, the triangular wave signals with amplitude of 2.5 V (2mm) and frequency of 5 Hz and 10 Hz were tracked, and the spectrum analysis of their errors was performed. The tracking results and fast fourier transform (FFT) of errors are shown in Fig. 8 and Fig. 9.

As shown in Fig. 8, the periodic error decreases with the increase of iteration period in the process of trajectory tracking, and the final error converges to ±0.01 mm, only 0.5% of the stroke.

Fig. 9 gives the FFT of tracking errors using compound control method when the tracking frequency is 10 Hz. And it is also compared with another controller. Obviously, the controller

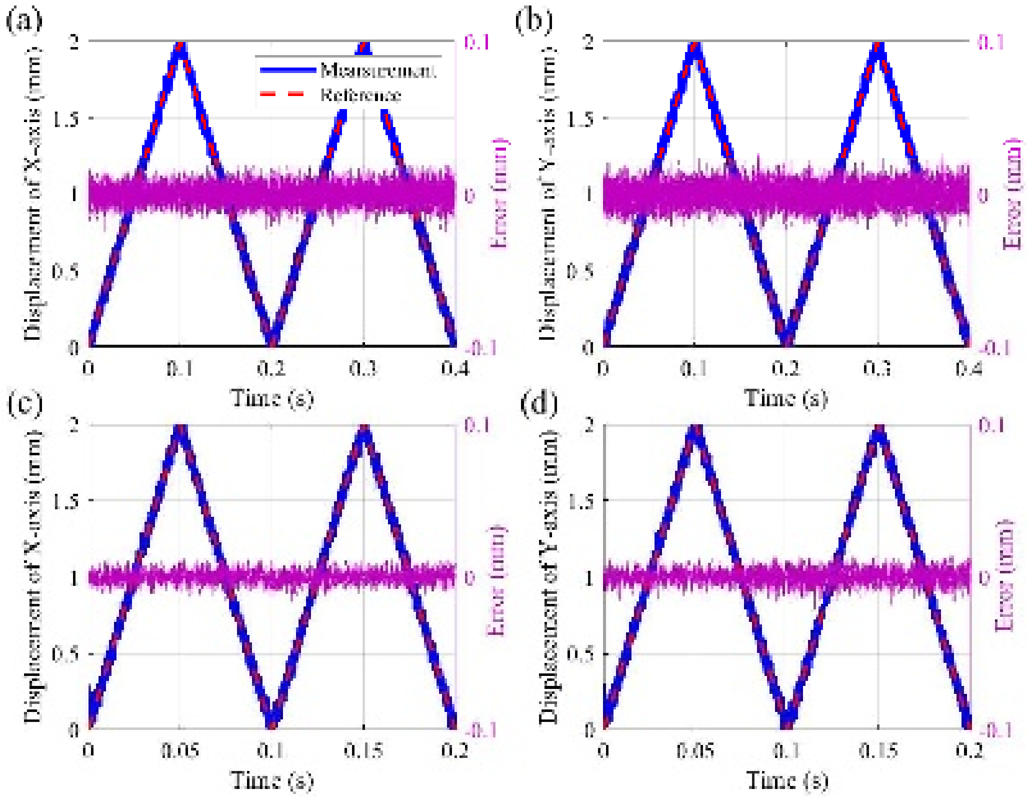

FIG. 8. Experimental results of tracking control. (a) and (b) are the tracking curves of X-axis or Y-axis of the stage when the frequency is 5 Hz respectively. (c) and (d) are the tracking curves of X-axis or Y-axis of the stage when the frequency is 10 Hz respectively

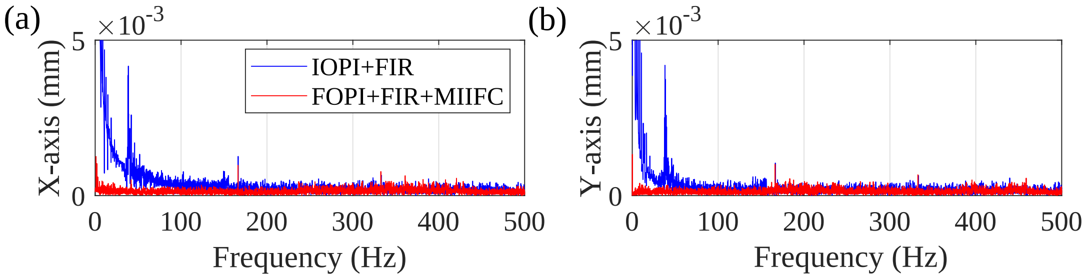

FIG. 9. The comparison of FFT of tracking error between the FOPI and FOPI+FIR+MIIFC controller at 10 Hz. (a) X-axis. (b) Y-axis

can compensate the high-order harmonic effectively. For the tracking trajectory of 10 Hz, the compound controller can compensate the fundamental wave to a large extent, eliminate the influence of noise signal on iteration, and achieve the high-precision control of the stage.

Finally, in order to comprehensively verify the performance of the designed 2-DOF large stroke flexure micro-positioning stage and the tracking effect of the proposed controller, tracking tests were conducted on complex trajectories such as concentric circle. The tracking results are shown in Fig. 10 which prove the excellent performance of the large stroke micropositioning stage and the effectiveness of proposed control method.

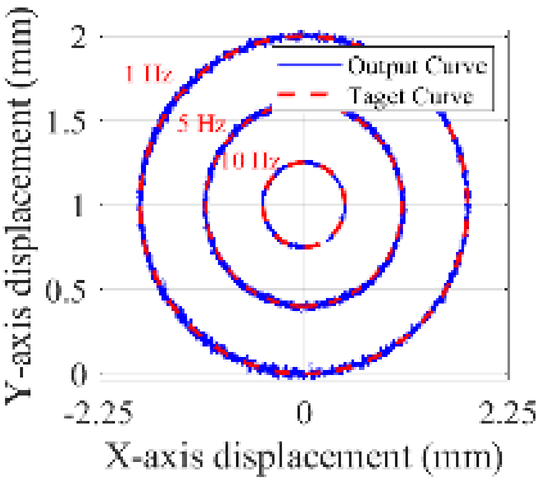

FIG. 10. Experimental results of complex curve tracking.

VI. CONCLUSION

In this paper, complex MIIFC, FIR filter and IFT control methods were proposed for the high-speed and high-precision control of stage. Firstly, the working principle of Maxwell reluctance actuator was introduced, and a large stroke reluctance-actuated micropositioning stage was constructed. Then, the input and output data were used to optimize and design FOPI controller and FIR filter. At the same time, the input and output data are used to estimate the system frequency response function online and carry out feedforward compensation to further eliminate the influence of resonance. Finally, the proposed method was compared with other conventional control methods to verify its effectiveness, and the tracking experiments were carried out on triangular wave trajectories with different frequencies. The experimental results show that the maximum tracking error of the control method for the desired trajectory of triangular wave is 0.5%, which effectively proves the effectiveness of the proposed method.

ACKNOWLEDGMENTS

This work was supported by the National Natural Science Foundation of China (Grant No. U2013211), the Natural Science Foundation of Shanghai (Grant No. 21ZR1426000), and the State Key Laboratory of Mechanical System and Vibration (Grant No. MSV202210).

REFERENCES

[1] C. Lee, J. W. Lee, S. G. Ryu, and J. H. Oh, "Optimum design of a large area flexure based xy0 mask alignment stage for a 12-inch wafer using grey relation analysis," Robotics & Computer Integrated Manufacturing **58**, 109–119 (2019).

[2] T. J. Teo, I. M. Chen, and G. Yang, "A large deflection and high payload flexure-based parallel manipulator for uv nanoimprint lithography: Part ii. stiffness modeling and performance evaluation," Precision Engineering **38**, 872–884 (2014).

[3] Y. Li and Q. Xu, "A novel piezoactuated xy stage with parallel, decoupled, and stacked flexure structure for micro/nanopositioning," IEEE Transactions on Industrial Electronics **58**, 3601–3615 (2011).

[4] M. Torralba, M. Valenzuela, J. Yagüe-Fabra, J. A. Albajez, and J. J. Aguilar, "Large range nanopositioning stage design: A three-layer and two-stage platform," Measurement **89**, 55–71 (2016).

[5] A. Okyay, K. Erkorkmaz, and M. B. Khamesee, "Mechatronic design, actuator optimization, and control of a long stroke linear nano-positioner," Precision Engineering **52**, 308–322 (2018).

[6] Y. Tian, K. Cai, D. Zhang, X. Liu, and B. Shirinzadeh, "Development of a xyz scanner for home-made atomic force microscope based on fpaa control," Mechanical Systems and Signal Processing **131**, 222–242 (2019).

[7] S. Ito, F. Cigarini, and G. Schitter, "Flux-controlled hybrid reluctance actuator for high-precision scanning motion," IEEE Transactions on Industrial Electronics **67**, 9593–9600 (2020).

[8] S. Ito, S. Troppmair, F. Cigarini, and G. Schitter, "High-speed scanner with nanometer resolution using a hybrid reluctance force actuator," IEEJ Journal of Industry Applications **8**, 170–176 (2019).

[9] E. Csencsics, J. Schlarp, and G. Schitter, "High-performance hybrid-reluctance-force-based tip/tilt system: Design, control, and evaluation," IEEE/ASME Transactions on Mechatronics **23**, 2494–2502 (2018).

[10] A. Safa, R. Y. Abdolmalaki, S. Shafiee, and B. Sadeghi, "Adaptive nonsingular terminal sliding mode controller for micro/nanopositioning systems driven by linear piezoelectric ceramic motors," ISA transactions **77**, 122–132 (2018).

[11] H. Ghafarirad, S. M. Rezaei, M. Zareinejad, and N. A. Mardi, "Charge-based hysteresis compensation in low impedance piezoelectric actuators by a modified prandtl–ishlinskii model:," Proceedings of the Institution of Mechanical Engineers, Part E: Journal of Process Mechanical Engineering **233**, 83–93 (2019).

[12] S. Ito, S. Troppmair, B. Lindner, F. Cigarini, and G. Schitter, "Long-range fast nanopositioner using nonlinearities of hybrid reluctance actuator for energy efficiency," IEEE Transactions on Industrial Electronics **66**, 3051–3059 (2019).

[13] Y. Tian, Y. Ma, F. Wang, K. Lu, and D. Zhang, "Control and testing of a serial-parallel xyz precision positioner with a discrete-time sliding model controller," IEEE Transactions on Control Systems Technology **21**, 1549–1557 (2019).

[14] X. Wang, L. Li, Z. Zhu, and L. Zhu, "Simultaneous damping and tracking control of a normal-stressed electromagnetic actuated nano-positioning stage," Sensors and Actuators A: Physical **338**, 113467 (2022).

[15] S. Xiao and Y. Li, "Optimal design, fabrication and control of an xy micro-positioning stage driven by electromagnetic actuators," IEEE Transactions on Industrial Electronics **60**, 4613–4626 (2013).

[16] Y. Qin, Y. Tian, D. Zhang, B. Shirinzadeh, and S. Fatikow, "A novel direct inverse modeling approach for hysteresis compensation of piezoelectric actuator in feedforward applications," IEEE/ASME Transactions on Mechatronics **18**, 981–989 (2013).

[17] S. Yu, J. Li, X. Lu, Y. Feng, and X. Sun, "Modeling-free inversion-based iterative feedforward control for piezoelectric actuators," in *2021 American Control Conference (ACC)* (IEEE, 2021) pp. 1396–1401.

[18] K.-S. Kim and Q. Zou, "A modeling-free inversion-based iterative feedforward control for precision output tracking of linear time-invariant systems," IEEE/ASME Transactions on Mechatronics **18**, 1767–1777 (2012).

[19]Y. Jiang, Y. Zhu, K. Yang, C. Hu, and D. Yu, "A data-driven iterative decoupling feedforward control strategy with application to an ultraprecision motion stage," IEEE Transactions on Industrial Electronics **62**, 620–627 (2015).

[20]G. Parmar, K. Barton, and S. Awtar, "Large dynamic range nanopositioning using iterative learning control," Precision Engineering **38**, 48–56 (2014).

[21]X. Zhang, L. Lai, L. Zhang, and L. Zhu, "Hysteresis and magnetic flux leakage of long stroke micro/nanopositioning electromagnetic actuator based on maxwell normal stress," Precision Engineering **75**, 1–11 (2022).

[22]H. Wu, L. Lai, L. Zhang, and L. Zhu, "Fractional order zero phase error tracking control of a novel decoupled 2-dof compliant micro-positioning stage," Journal of Micromechanics and Microengineering **31**, 105006 (2021).

[23]M. Ghorbani and M. Tavakoli-Kakhki, "Robust stabilizability of fractional order proportional integral controllers for fractional order plants with uncertain parameters: A new value set based approach," Journal of Vibration and Control **26**, 965–975 (2020).

[24]A. Oustaloup, F. Levron, B. Mathieu, and F. M. Nanot, "Frequency-band complex noninteger differentiator: characterization and synthesis," IEEE Transactions on Circuits & Systems I Fundamental Theory & Applications **47**, 25–39 (2002).

[25]M. Omidbeike, A. A. Eielsen, Y. K. Yong, and A. J. Fleming, "Multivariable modelless feedforward control of a monolithic nanopositioning stage with fir filter inversion," in *2019 International Conference on Manipulation, Automation and Robotics at Small Scales (MARSS)* (2019) pp. 1–6.

[26]D. Kalaiyarasi and T. K. Reddy, "An efficient implementation of least mean square adaptive fir filter based on distributed arithmetic," Far East Journal of Electronics and Communications **19**, 9–32 (2019).

[27]Y. Tian, Z. Huo, F. Wang, B. Shi, and D. Zhang, "Design and modeling of a decoupled 2-dof stick-slip positioning stage," in *2019 IEEE International Conference on Manipulation, Manufacturing and Measurement on the Nanoscale (3M-NANO)* (2019) pp. 211–215.

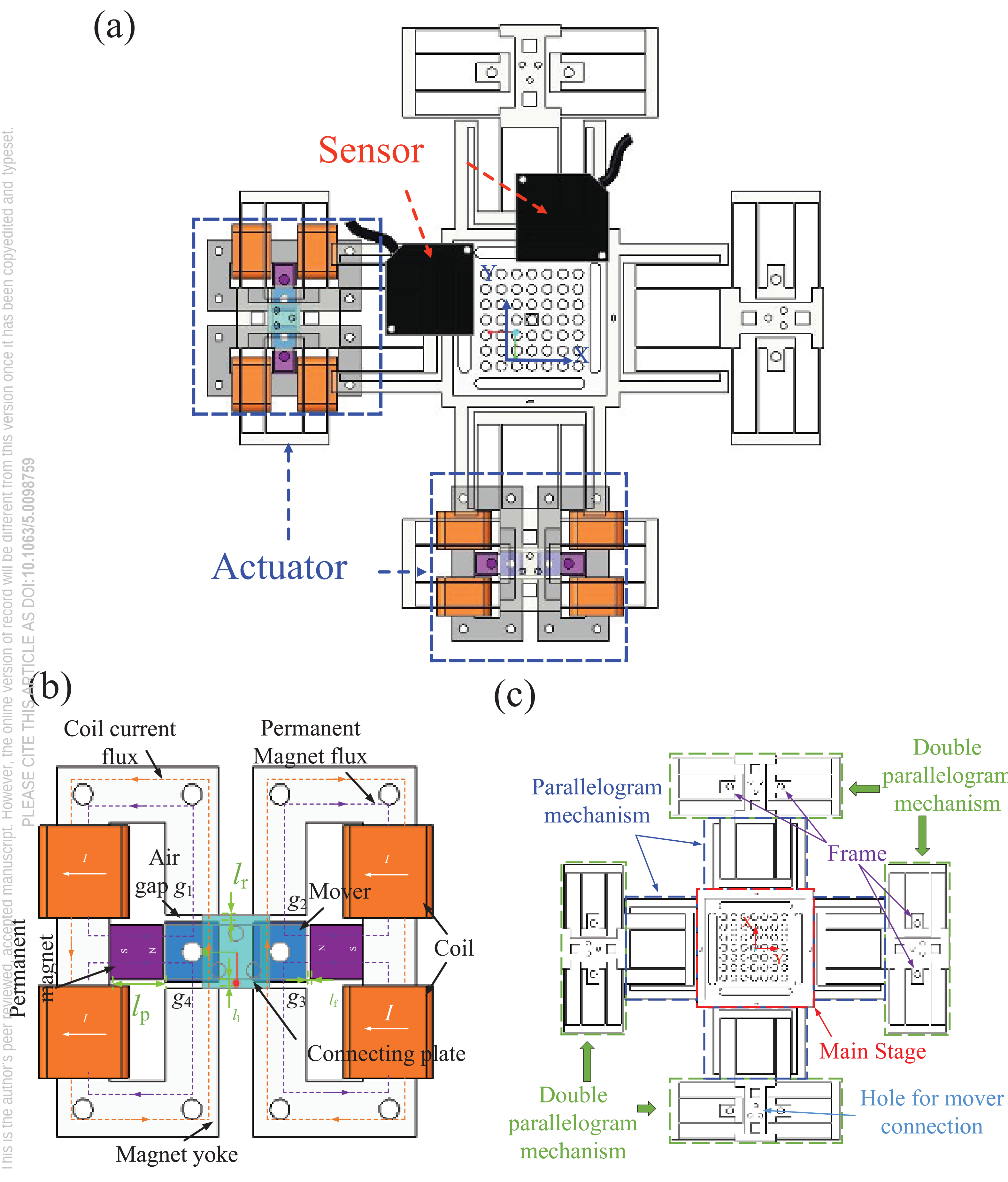
(a)
Sensor
Y
X
Actuator
(b)
Coil current flux
Permanent Magnet flux
Air gap g_1
g_2
Mover
l_r
Coil
Permanent magnet
l_p
g_4
g_3
l_f
l_l
I
S
N
Connecting plate
Magnet yoke
(c)
Parallelogram mechanism
Double parallelogram mechanism
Frame
X
Y
Main Stage
Double parallelogram mechanism
Hole for mover connection

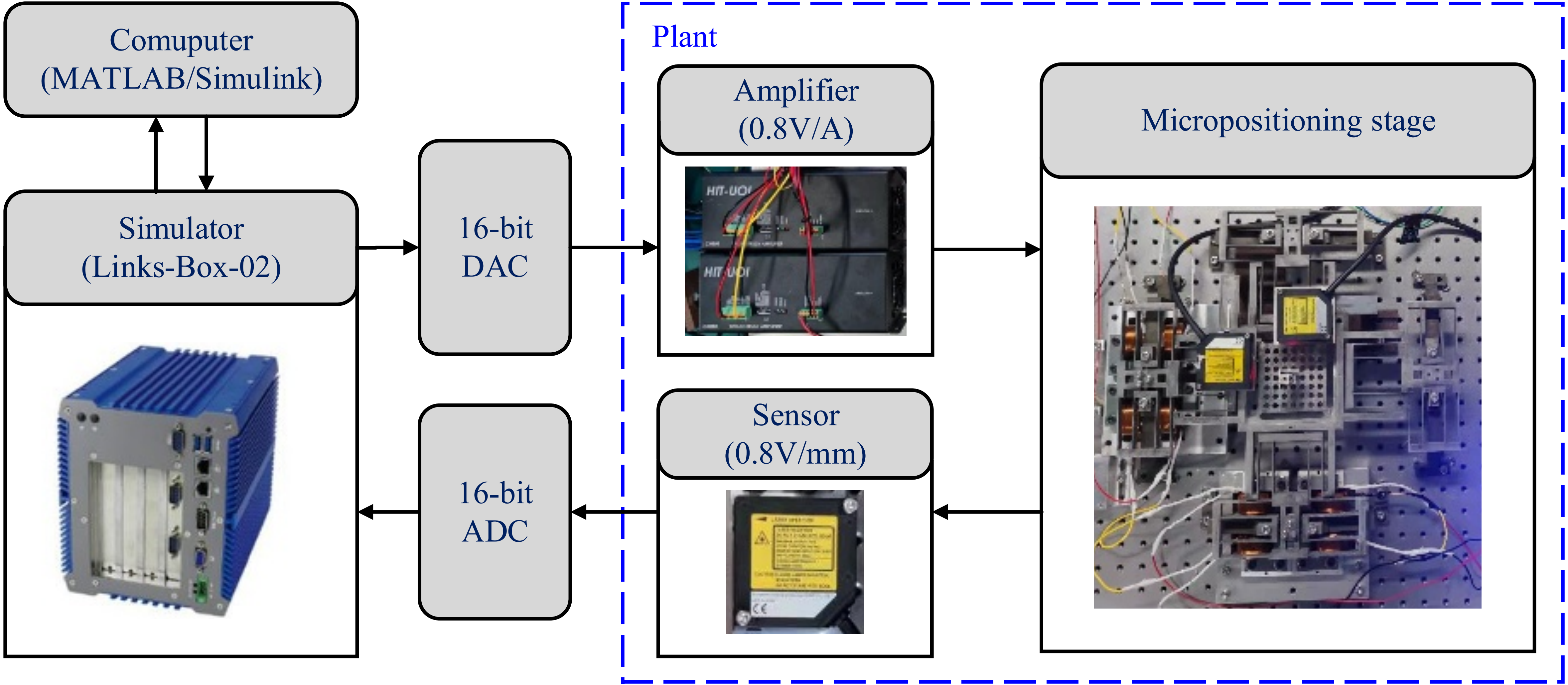
Comuputer
(MATLAB/Simulink)
Simulator
(Links-Box-02)
16-bit
DAC
16-bit
ADC
Plant
Amplifier
(0.8V/A)
HIT-UOI
HIT-UOI
Micropositioning stage
Sensor
(0.8V/mm)

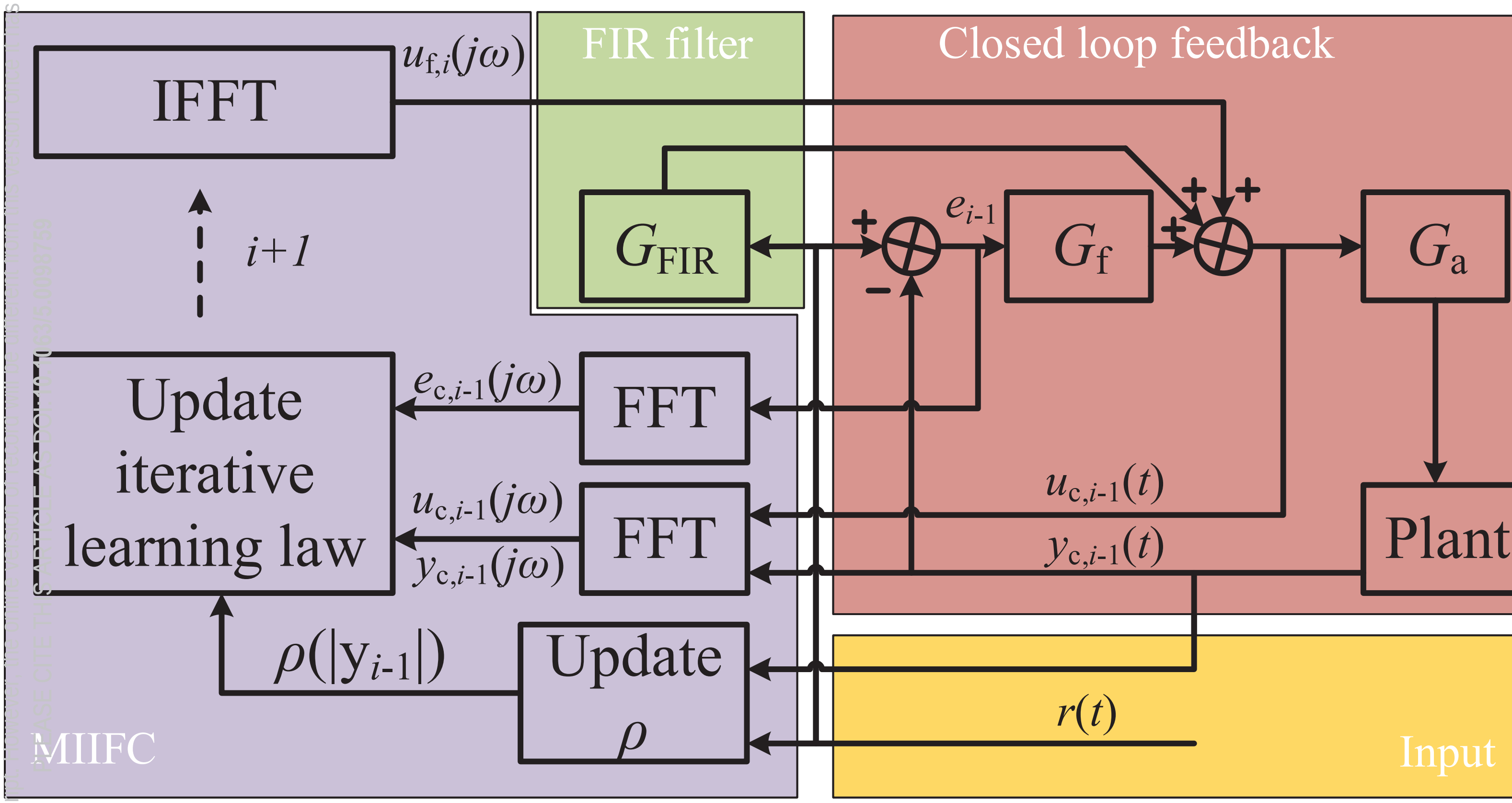
FIR filter
Closed loop feedback
IFFT
$u_{f,i}(j\omega)$
$i+1$
G_{FIR}
+
−
e_{i-1}
G_f
+
+
+
G_a
Update iterative learning law
$e_{c,i-1}(j\omega)$
FFT
$u_{c,i-1}(j\omega)$
$y_{c,i-1}(j\omega)$
FFT
$u_{c,i-1}(t)$
$y_{c,i-1}(t)$
Plant
$\rho(|y_{i-1}|)$
Update ρ
$r(t)$
MIIFC
Input

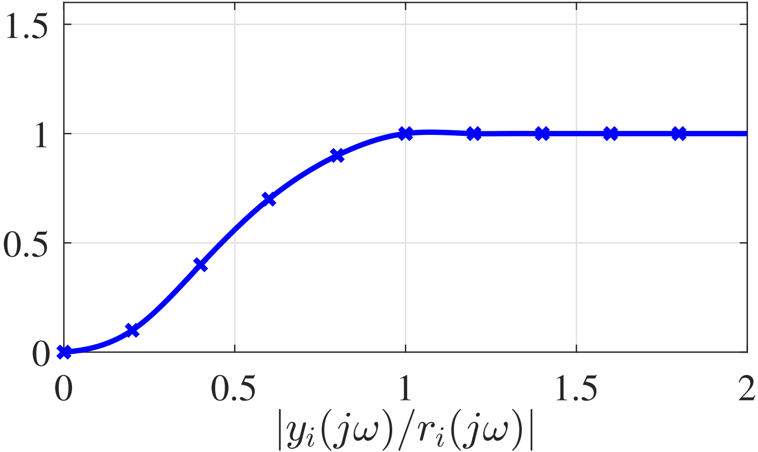

$\rho(y_i)$
1.5
1
0.5
0
0
0.5
1
1.5
2
$|y_i(j\omega)/r_i(j\omega)|$

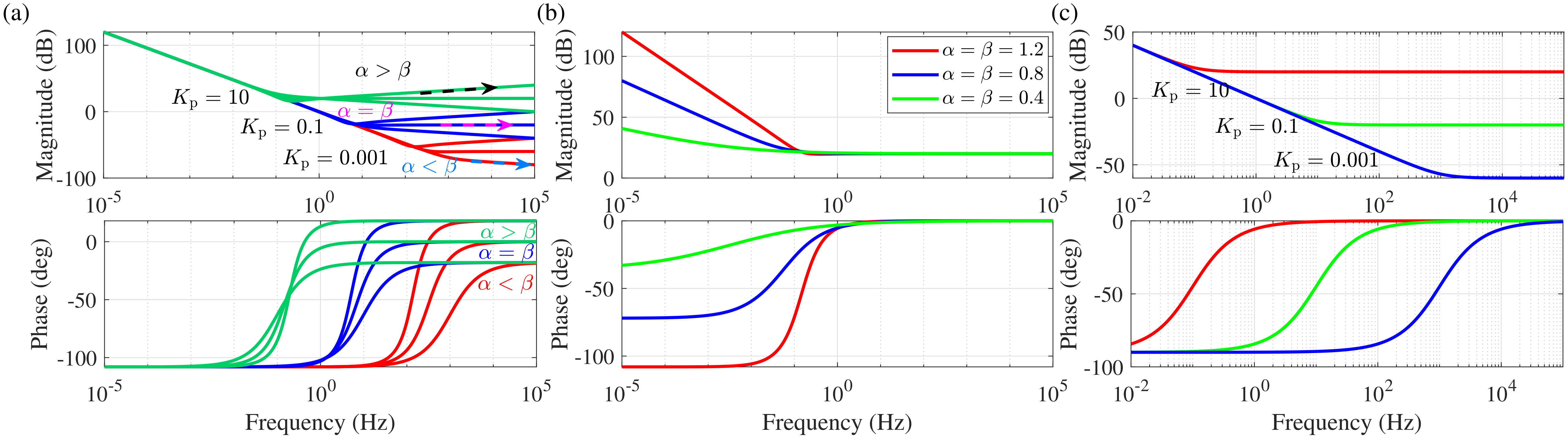
(a)
Magnitude (dB)
100
0
-100
$\alpha > \beta$
$K_\mathrm{p} = 10$
$\alpha = \beta$
$K_\mathrm{p} = 0.1$
$K_\mathrm{p} = 0.001$
$\alpha < \beta$
10^{-5}
10^{0}
10^{5}
Phase (deg)
0
-50
-100
$\alpha > \beta$
$\alpha = \beta$
$\alpha < \beta$
10^{-5}
10^{0}
10^{5}
Frequency (Hz)
(b)
Magnitude (dB)
100
50
0
$\alpha = \beta = 1.2$
$\alpha = \beta = 0.8$
$\alpha = \beta = 0.4$
10^{-5}
10^{0}
10^{5}
Phase (deg)
0
-50
-100
10^{-5}
10^{0}
10^{5}
Frequency (Hz)
(c)
Magnitude (dB)
50
0
-50
$K_\mathrm{p} = 10$
$K_\mathrm{p} = 0.1$
$K_\mathrm{p} = 0.001$
10^{-2}
10^{0}
10^{2}
10^{4}
Phase (deg)
0
-50
-100
10^{-2}
10^{0}
10^{2}
10^{4}
Frequency (Hz)

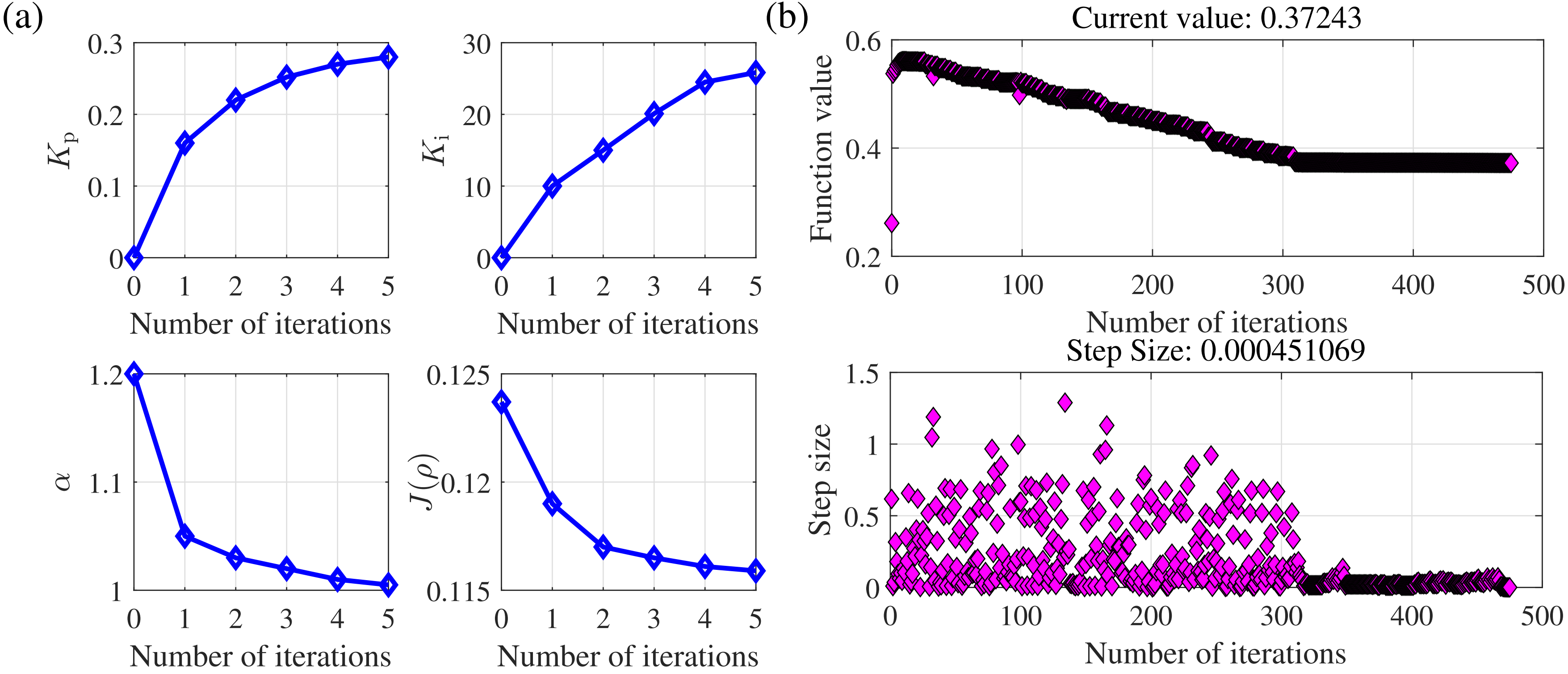
(a)
K_p
0
0.1
0.2
0.3
0 1 2 3 4 5
Number of iterations
K_i
0
10
20
30
0 1 2 3 4 5
Number of iterations
α
1
1.1
1.2
0 1 2 3 4 5
Number of iterations
$J(\rho)$
0.115
0.12
0.125
0 1 2 3 4 5
Number of iterations
(b)
Current value: 0.37243
Function value
0.2
0.4
0.6
0 100 200 300 400 500
Number of iterations
Step Size: 0.000451069
Step size
0
0.5
1
1.5
0 100 200 300 400 500
Number of iterations

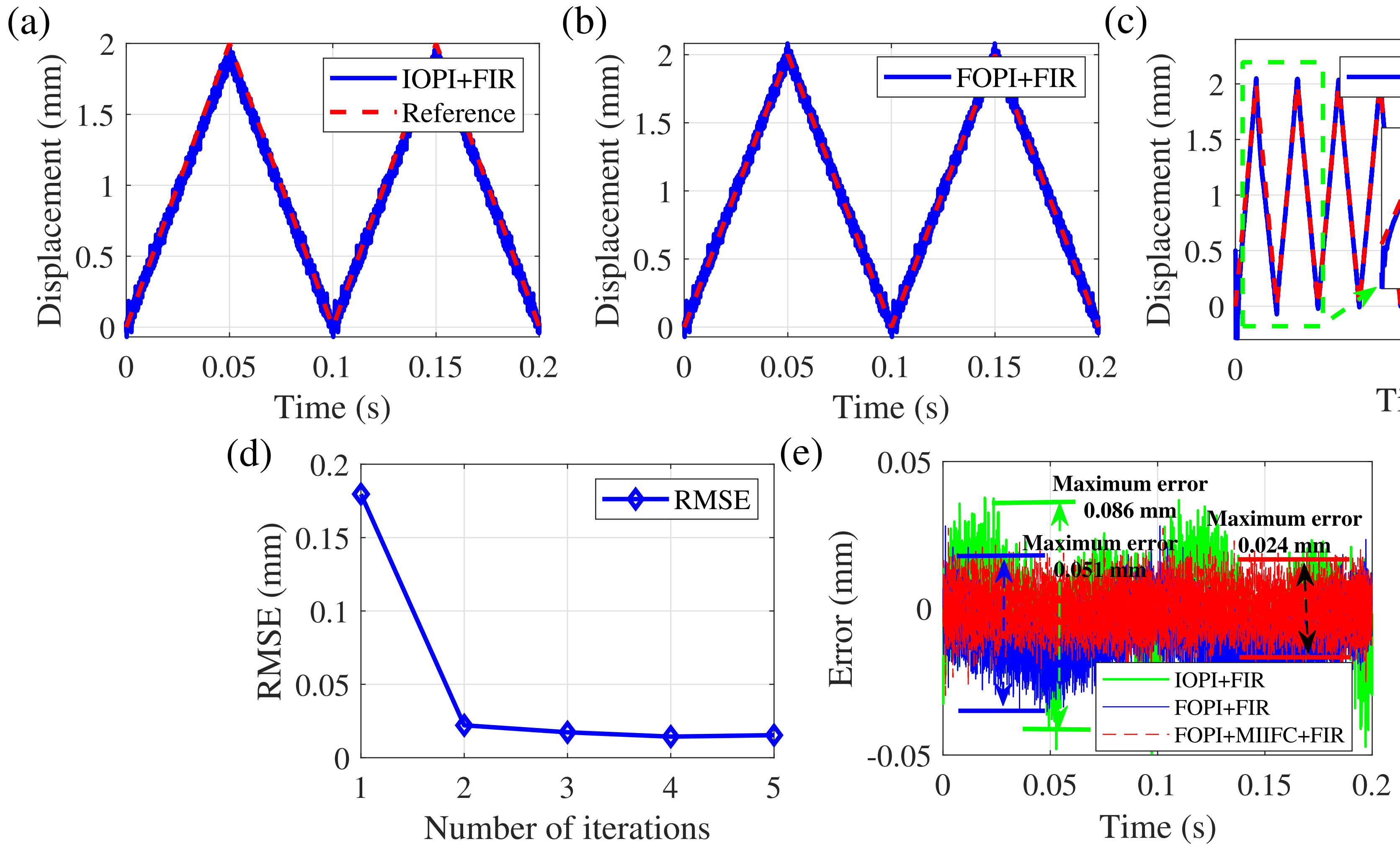
(a)
IOPI+FIR
Reference
Displacement (mm)
Time (s)
0
0.5
1
1.5
2
0.05
0.1
0.15
0.2
(b)
FOPI+FIR
Displacement (mm)
Time (s)
(c)
FOPI+MIIFC+FIR
Displacement (mm)
Time (s)
0.5
1
(d)
RMSE
RMSE (mm)
Number of iterations
0.2
0.15
0.1
0.05
0
1
2
3
4
5
(e)
Maximum error
0.086 mm
Maximum error
0.051 mm
Maximum error
0.024 mm
IOPI+FIR
FOPI+FIR
FOPI+MIIFC+FIR
Error (mm)
Time (s)
0.05
0
-0.05
0.05
0.1
0.15
0.2

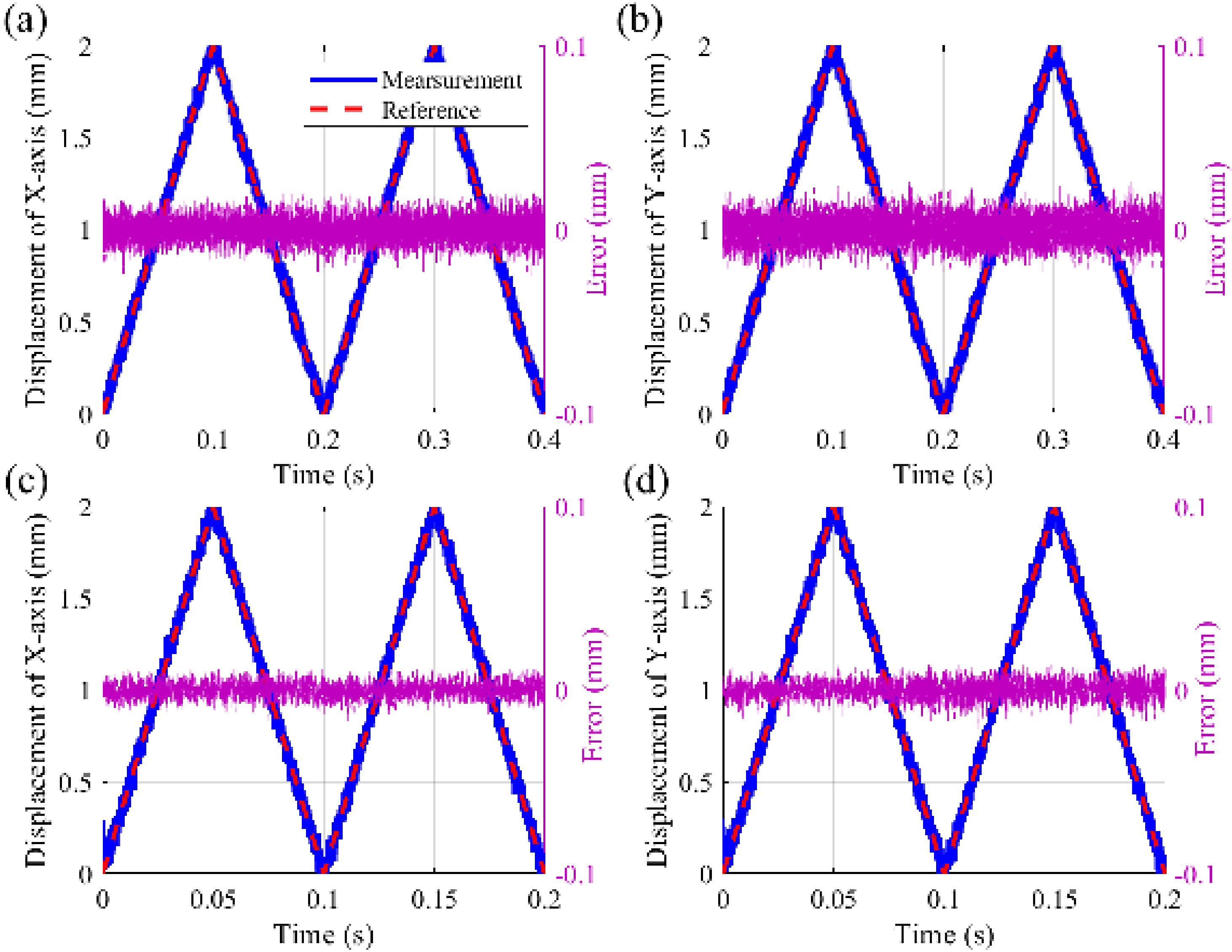
(a)
Displacement of X-axis (mm)
Error (mm)
Time (s)
Mearsurement
Reference
0
0.5
1
1.5
2
0.1
0
-0.1
0.1
0.2
0.3
0.4
(b)
Displacement of Y-axis (mm)
Error (mm)
Time (s)
(c)
Displacement of X-axis (mm)
Error (mm)
Time (s)
0.05
0.15
(d)
Displacement of Y-axis (mm)
Error (mm)
Time (s)

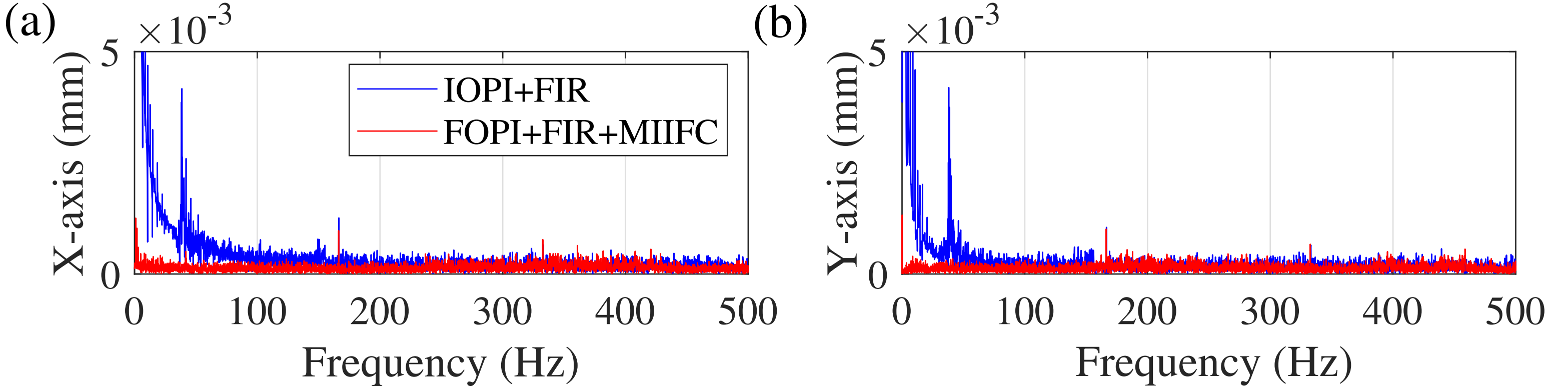
(a)
×10⁻³
5
0
X-axis (mm)
IOPI+FIR
FOPI+FIR+MIIFC
0
100
200
300
400
500
Frequency (Hz)
(b)
×10⁻³
5
0
Y-axis (mm)
0
100
200
300
400
500
Frequency (Hz)

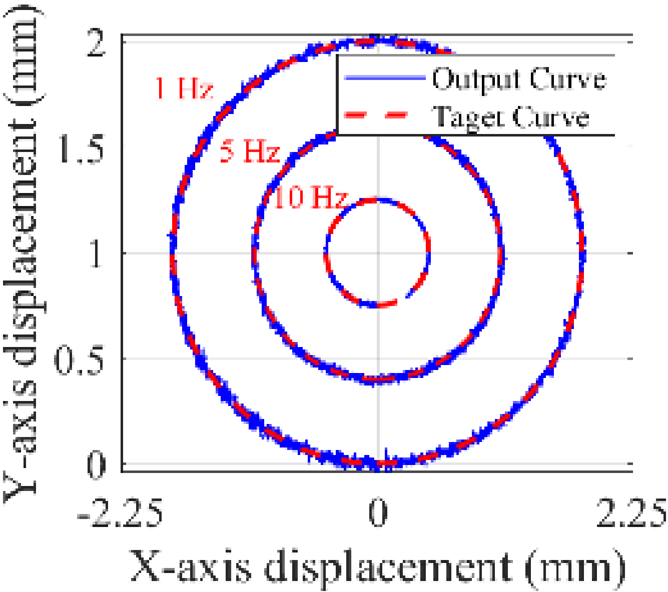
Output Curve
Taget Curve
1 Hz
5 Hz
10 Hz
Y-axis displacement (mm)
2
1.5
1
0.5
0
-2.25
0
2.25
X-axis displacement (mm)